

SpyroPose: Importance Sampling Pyramids for Object Pose Distribution Estimation in SE(3)

Rasmus Laurvig Haugaard

Frederik Hagelskjær

Thorbjørn Mosekjær Iversen

SDU Robotics, University of Southern Denmark

{rlha, frhag, thmi}@mmmi.sdu.dk

Abstract

Object pose estimation is a core computer vision problem and often an essential component in robotics. Pose estimation is usually approached by seeking the single best estimate of an object’s pose, but this approach is ill-suited for tasks involving visual ambiguity. In such cases it is desirable to estimate the uncertainty as a pose distribution to allow downstream tasks to make informed decisions. Pose distributions can have arbitrary complexity which motivates estimating unparameterized distributions, however, until now they have only been used for orientation estimation on $SO(3)$ due to the difficulty in training on and normalizing over $SE(3)$. We propose a novel method for pose distribution estimation on $SE(3)$. We use a hierarchical grid, a pyramid, which enables efficient importance sampling during training and sparse evaluation of the pyramid at inference, allowing real time 6D pose distribution estimation. Our method outperforms state-of-the-art methods on $SO(3)$, and to the best of our knowledge, we provide the first quantitative results on pose distribution estimation on $SE(3)$. Code will be available at [spyropose.github.io](https://github.com/spyropose)

1. Introduction

Many tasks in robotics involving manipulation of rigid objects require that an object’s rotation and translation, referred to as the object’s 6D pose, is known. Vision systems are often relied upon to estimate object poses when the environment is relatively uncontrolled, such as when objects lies cluttered on a table or in a bin. Since pose estimation is such a crucial but also challenging task, it is not surprising that the topic is well studied in the literature.

Most of the pose estimation literature has been dedicated to algorithms which provide a single “best guess” of the pose. However, while a single estimate can be adequate in many scenarios, there are also many real world tasks that involve visual ambiguity, e.g. due to occlusions or object symmetries. When pose estimation is confined to a point

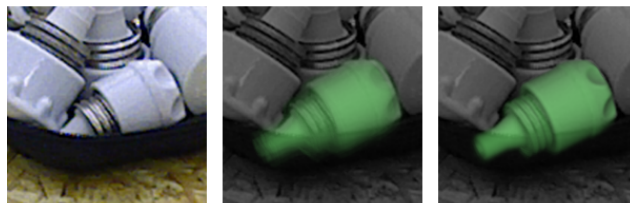
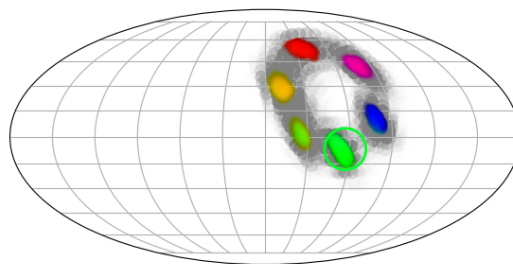


Figure 1. Visualization of SE(3) distributions at different levels of the SE(3) pyramid. The input image is shown in the bottom left. Renders of SE(3) poses, weighted by their probability are shown next to the input image for recursion 3 and 5. At the top, the marginalized rotational distribution is shown using a Mollweide projection with the last dimension represented by color. For clarity, recursion 3 is shown grayscale and recursion 5 in colors. The true rotation is marked with a circle.

estimate, the vision system is by design limited in its capabilities to express uncertainty.

Unlike “best pose” estimation, pose distribution estimation seeks to estimate an entire probability distribution over object poses defined on $SE(3)$. Allowing and representing visual uncertainties facilitates more informed, principled interactions between computer vision and robotics. This has e.g. been shown in [7], where the vision uncertainty represented as normal and success thresholds on a grasping task are combined to estimate the success of a grasp in a constrained environment. However, research into more subtle interactions between robotic control and visual uncertainties has been limited due to the lack of a reliable method for estimating complex probability distributions on $SE(3)$.

There are many ways to model probability distributions, including mixture models of parameterized functions, histograms, weighted ensembles of particles, and implicit functions. Implicit functions are especially interesting due to their ability to express arbitrary distributions and they have been used successfully to estimate distributions on $SO(3)$ [21] using a contrastive loss with uniformly sampled negatives during training and a uniform grid during inference. There are two problems with extending this method to $SE(3)$. Firstly, uniformly sampled negatives provides less information as the space grows from $SO(3)$ to $SE(3)$, and secondly, evaluation of a uniform grid on $SE(3)$ becomes prohibitively expensive at any practical resolution.

We present SpyroPose, a novel method for real time pose distribution estimation on $SE(3)$. See Fig. 1. Our method is based on three key principles:

- Importance sampling during training using an $SE(3)$ hierarchical grid, or pyramid, which provides hard negatives and lower variance estimates of the partition function.
- Sparse evaluation of the pyramid at inference, reducing the number of required evaluations by several orders of magnitude, enabling real time pose distribution estimation, even on CPU.
- Keypoint feature extraction, inducing a camera model bias into the model to enable translational equivariance and to avoid relying on a single latent embedding to represent complex, high-resolution distributions.

We present state-of-the-art rotation distribution estimation results on SYMSOL [21] and to the best of our knowledge, we present the first quantitative results on distribution estimation on $SE(3)$.

2. Related Work

Handling visual ambiguities is a challenging part of object pose estimation. Most work [30, 26, 24, 19] on pose estimation uses manual annotations to explicitly handle one cause of visual ambiguity, symmetries, and infers a “best guess” pose estimate without expressing uncertainty. The defacto pose estimation benchmark, BOP [13], is also centered around point estimates and known object symmetries.

Some methods [11, 8] that provide point estimates do however handle visual ambiguities in a principled way. EPOS [11] regresses dense, per pixel, histograms of object surface regions to obtain 2D-3D correspondences and use them in a PnP-RANSAC framework to provide pose estimates without knowing about symmetries a priori. SurfEmb [8] extends this idea and estimates dense full 2D-3D correspondence distributions. However, the dense correspondence histograms and -distributions have not been shown to be useful to model pose distributions.

There are also pose estimation methods that represent uncertainties. In [28], model ensembles are used to estimate epistemic uncertainty which indicate a degree of generalization uncertainty caused by insufficient training data or a domain gap. This however does not help represent the inherent aleatoric ambiguities in pose estimation, which could be used in down stream tasks or for sensor fusion.

Work on modeling the aleatoric uncertainty has traditionally been approached with parametric distributions. The most common parametric model of uncertainty is the multivariate normal distribution. Early work has focused on propagating correspondence uncertainties to pose space for classical pose estimation methods such as ICP [1] and PnP [4], which assume that the correspondence ambiguities are Gaussian, however, even simple symmetries and occlusions breaks this assumption.

Since orientation and position are defined on different manifolds, $SO(3)$ and \mathbb{R}^3 , respectively, it has been custom to assume them to be decoupled and treat the two parts separately, usually assuming the position to be normal. Bingham is the most popular parametric distribution for modeling orientation uncertainty. The estimation of the parameters of a Bingham mixture model has been done in various ways, including deep learning based regression [22, 2, 5], and fitting a Bingham mixture model to an ensemble of pose hypotheses [20]. Additionally, [25] shows that the parameters of a von Mises mixture model can be estimated.

Finally, there are works on unparametric distributions on $SO(3)$. [22, 17] directly regress a rotation histogram which is able to represent arbitrary distributions at a coarse resolution, but the generalization across bins is limited, requiring all bins to be well represented in the training data, making it difficult to scale the histogram to higher resolution, not to mention $SE(3)$. [29, 3] trains a denoising autoencoder on image crops and uses cosine similarities on the learnt latent embeddings to estimate visual ambiguities. However, since the loss is a reconstruction loss, and the distribution is designed, the estimated distributions are heuristic.

Recently, a number of methods has been proposed which model the unparametric distributions implicitly. In [15], the marginal distributions of keypoint projections are estimated across the image which can provide a conservative estimate of unnormalized pose likelihoods, however, the capacity of the model is limited because the joint distribution of keypoints is not modeled. Their method could also be used for 6D pose distribution estimation, however, they only present results on rotation distribution estimation due to the lack of a method to normalize over $SE(3)$. ImplicitPDF [21], which has inspired this work, trains a Multi Layer Perceptron (MLP) to map an image embedding and a rotation to an unnormalized likelihood. They show a single qualitative result on 6D object pose distribution estimation on simple synthetic data in their supplementary material, however, no

quantitative results are shown. HyperPosePDF [14] is similar, but instead of estimating a latent embedding from an image and feeding it to an MLP, they learn a mapping from an image to the weights of an MLP which maps rotations to unnormalized likelihoods. I2S [18] is also similar, but maps features from the image domain to SO(3) followed by SO(3) equivariant layers, before mapping to the unnormalized rotation likelihood. They show good generalization capabilities but lower resolution than the related methods.

Like [21, 14, 18], we also use an implicit formulation to estimate unnormalized log likelihoods, however, we use a hierarchical grid, or pyramid, in SE(3) which combined with importance sampling allows us to learn unparameterized distributions in SE(3), and the same pyramid is used at inference, enabling real time pose distribution estimation. We also make use of the spatial dimensions of the image in our latent pose distribution embedding, to relieve a single image embedding to represent complex, high-resolution distributions.

3. Methods

At its core, our method is based on learning pose distributions at different levels of resolution. Given a pose hypothesis, we project object keypoints into the image, extract image features at the projected points and feed the sampled features to resolution-specific Multi Layer Perceptrons (MLPs). At inference, this allows a very sparse top-down evaluation of a pyramid of poses, only expanding the most likely poses to the next, higher-resolution level. During training, having models at different resolutions allows us to sample negatives from a pose distribution which is closer to the desired distribution than uniform, enabling importance sampling to provide better signal to the high-resolution layers. The following provides details of our method.

3.1. Problem Definition

Given an image $I \in \mathbb{R}^{H \times W \times C}$ of an object of interest, we aim to estimate the conditional distribution, $p(x|I)$, of the object’s 6D pose, $x \in \text{SE}(3)$. The distribution should be unparameterized, i.e., not assuming position and orientation to be decoupled, and without assuming the distribution to be of a certain family or with a certain number of modes. The distributions should also be correctly normalized, and to have most practical value, the learnt distribution estimates should both be of high resolution and be obtained in real time.

3.2. SE(3) Pyramid Definition

We use an equivolumetric hierarchical grid in SE(3), which we’ll refer to as an SE(3) pyramid. The pyramid is the cartesian product between a positional grid in \mathbb{R}^3 and rotational grid in SO(3).

For the rotational part of the pyramid, we use the HealPix grid [6] extended to SO(3) by [31]. Like previous work [21, 14, 15] we use the grid for its equivolumetric property, however, unlike previous work we also use its hierarchical structure: Let $R^{(r)} \subset \text{SO}(3)$ denote the grid of rotations at recursion r , and $R_i^{(r)} \in R^{(r)}$ a cell in the grid. At the coarsest level, recursion level 0, there are 72 rotations, $|R^{(0)}| = 72$. For each recursion, each rotation in the grid is split into 8 rotations, $|R^{(r)}| = 72 \cdot 8^r$. The volume of the grid is $V(R^{(r)}) = \pi^2$ and because the grid is equivolumetric, a cell in the rotational grid has volume $V(R_i^{(r)}) = \pi^2 / (72 \cdot 8^r)$.

For the positional part, we need to define the bounds of the grid, since \mathbb{R}^3 is not bounded. We define the bounds in two steps. In the first step the positional error is modeled using a conservative estimate of visual ambiguity to ensure that the true pose is within the estimated bounds. In the second step, a hierarchical grid is defined such that it fully encompasses the conservatively estimated positional distribution. Let $\hat{t} \in \mathbb{R}^{3 \times 1}$ be a coarse estimate of the object’s position, t . Depending on the application, this estimate could come from a detector, be known a priori, or obtained otherwise. In the following, we assume \hat{t} to come from a detector. We then define a large bound on t based on \hat{t} . Specifically, we presume that the maximum magnitude of the perceived positional ambiguity is equal to the object’s radius. Let d be the diameter of the object of interest. Then parallel to the image plane, we let the error be up to $d/2$. Along the view direction, we let the object’s distance to the camera be down to half, which assuming a pinhole camera model would cause the appeared size to be doubled.

Formally, we define a bound which meets the above criteria by introducing a truncated multivariate normal variable, $\tilde{e} = \mathcal{N}(0, \sigma I, 1/2)$, where ”1/2” indicates, that its truncated at $\|\tilde{e}\|_2 = 1/2$, and then define our random error variable e as

$$e = A\tilde{e}, \quad A = \begin{bmatrix} d & 0 & \hat{t}_x \\ 0 & d & \hat{t}_y \\ 0 & 0 & \hat{t}_z \end{bmatrix}. \quad (1)$$

The resulting bound of $\tilde{t} = \hat{t} + e$ is a sphere centered around \hat{t} and elongated along the view direction, encompassing more depth- than in-plane ambiguity.

We define the positional grid, $p^{(r)} \in \mathbb{R}^{3 \times N}$, with $N = 8^r$ at recursion r as

$$p^{(r)} = \hat{t} + Ag^{(r)}, \quad (2)$$

where $g^{(r)} \in \mathbb{R}^{3 \times N}$ consists of the centers of the cubes in the 2^r by 2^r by 2^r regular grid inside an origo-centered unit cube. Note that $p^{(r)}$ encompasses \hat{t} , since $g^{(r)}$ encompasses \tilde{e} . Also note, that $p^{(r)}$ is hierarchical and equivolumetric, since $g^{(r)}$ is hierarchical and equivolumetric and $g^{(r)} \mapsto$

$\hat{t} + Ag^{(r)}$ is an affine transformation. The volume of the grid is $V(p^{(r)}) = \det(A)$, since the volume of $g^{(r)}$ is 1. The volume of a cell in $p^{(r)}$ is thus $V(p_i^{(r)}) = \det(A)/8^r$.

The SE(3) pyramid is simply the cartesian product of the positional and rotational grid, however, we must choose at which recursion to align them. At $R^{(0)}$, the angular distance to the nearest neighbour is approximately $\phi = 1$ rad, causing a visual effect of up to approximately $\phi d/2 = d/2$. Since $p^{(1)}$ has the same visual resolution, we define recursion 0 of the SE(3) pyramid, $x^{(0)}$, to be the cartesian product of $R^{(0)}$ and $p^{(1)}$: $x^{(0)} = R^{(0)} \times p^{(1)}$. Since $x^{(r)}$ is also an equivolumetric grid, it follows that

$$V(x_i^{(r)}) = \frac{V(x^{(r)})}{|x^{(r)}|} = \frac{\det(A)\pi^2}{(72+8)64^r}. \quad (3)$$

To prevent our models from learning the structure of a fixed SE(3) grid, we randomly offset and rotate $p^{(1)}$ and $R^{(0)}$ during training. For the rotational grid, we simply rotate $R^{(0)}$ by a random rotation during training, and for the positional grid, we let $p^{(r)} = \hat{t} + AR(g^{(r)} + s)$, where $s \in \mathbb{R}^{3 \times 1}$ and $R \in \text{SO}(3)$, making sure to extend $g^{(r)}$ to make $p^{(r)}$ encompass \hat{t} .

3.3. Contrastive Loss

The InfoNCE loss was presented in [23], inspired by Noise Contrastive Estimation,

$$L_{\text{InfoNCE}} = - \mathbb{E}_{x, I, X} \left[\log \frac{f_{\theta}(x, I)}{f_{\theta}(x, I) + \sum_{x_j \in X} f_{\theta}(x_j, I)} \right], \quad (4)$$

where (x, I) is sampled from the data distribution $p(x, I)$, θ are the parameters of the model, and X is a set of N samples from a noise distribution, $x_j \sim p_n(x)$. They show that for any N the loss leads to approximating $f_{\theta}(x, I) \propto p(x|I)p_n(x)^{-1}$, and it follows that letting the noise distribution be uniform, f_{θ} approximates an unnormalized distribution, $f_{\theta}(x|I) = \tilde{p}(x|I; \theta) \propto p(x|I)$.

Note that the last term in the denominator in Eq. (4), $\hat{Z} = \sum_{x_j \in X} f_{\theta}(x_j, I)$, is proportional to an unbiased estimate of the partition function, $\mathbb{E}_X \hat{Z} \propto \int f_{\theta}(x, I) dx$. An inherent problem with scaling the noise contrastive loss to higher dimensions is that the variance of the partition function estimate becomes higher given the same number of samples, due to the curse of dimensionality.

Importance sampling could be used to lower the variance of the estimate of the partition function, but it requires a heavy-tailed distribution close to $p(x|I; \theta)$ which can be sampled from with known sample likelihoods, and such a distribution is generally not available. However, in the next section we show how learning distributions at different resolutions can enable importance sampling.

3.4. Pyramid Models & Importance Sampling

Instead of learning $p(x|I; \theta)$ directly, we learn the distribution at different resolutions, one for each level in the pyramid, $p(x_i^{(r)}|I; \theta^{(r)})$. For a model at recursion r , we can then use the coarser models to provide an estimate of $p(x_i^{(r)}|I; \theta^{(r)})$ which can be used for importance sampling. We use the loss in Eq.(4) and map the true pose, x , to the nearest cell in $x^{(r)}$ to provide the positive in the numerator.

Let $P(x_i^{(r)}) = x_{i \setminus 64}^{(r-1)}$ be the parent of $x_i^{(r)}$ in the previous recursion, where \setminus denotes integer division, and let $C(x_i^{(r)}) = \{x_{64i+0}^{(r+1)}, \dots, x_{64i+63}^{(r+1)}\}$ be the set of children of $x_i^{(r)}$ in the next recursion. The siblings of $x_i^{(r)}$, including $x_i^{(r)}$ is thus $S(x_i^{(r)}) = C(P(x_i^{(r)}))$, and let $S(x_i^{(0)}) = x^{(0)}$. We then denote the relative probability among siblings as

$$q(x_i^{(r)}|I) = \frac{\tilde{p}(x_i^{(r)}|I)}{\sum_{x_j^{(r)} \in S(x_i^{(r)})} \tilde{p}(x_j^{(r)}|I)}. \quad (5)$$

With the true pyramid models, $p(x_i^{(r)}|I)$, $p(x|I)$ can be efficiently sampled from to arbitrary resolution by sampling a trajectory through the pyramid:

$$\bar{p}(x_i^{(r)}) = q(x_{i \setminus 64^r}^{(0)})q(x_{i \setminus 64^{r-1}}^{(1)}) \cdots q(x_{i \setminus 64}^{(r-1)}) \frac{1}{64}, \quad (6)$$

where conditioning on I is assumed and left out for clarity. Note that $\sum_{x_i^{(r)} \in x^{(r)}} \bar{p}(x_i^{(r)}) = 1$. Because we randomly offset the grids during training, there's an inherent ambiguity at the boundaries of the grid cells at each level, causing $\bar{p}(x_i^{(r)}|I)$ to be a heavy-tailed approximation of $p(x_i^{(r)}|I)$ at convergence. In the InfoNCE loss in Eq.(4) we can thus use $\bar{p}(x_i^{(r)}|I)$ as our importance sampling distribution,

$$\hat{Z}_{\text{IS}} = \sum_{x_i^{(r)} \in X} \frac{\tilde{p}(x_i^{(r)})}{\bar{p}(x_i^{(r)})}, \quad x_i^{(r)} \sim \bar{p}(x_i^{(r)}), \quad (7)$$

which is also proportional to an unbiased estimate of the partition function, but with lower variance, assuming $\bar{p}(x_i^{(r)}|I)$ is a better estimate of $p(x_i^{(r)}|I)$ than uniform. We could sample from $\bar{p}(x_i^{(r)}|I)$ independently at each recursion, but for efficiency, we use all the evaluated siblings at each recursion in n trajectories through the whole pyramid, amounting to $|x^{(0)}|$ evaluations for the first layer and $64n$ evaluations for subsequent layers.

Note that we could maximize the log likelihood directly, normalized by our importance sampling partition function estimate, but initial experiments showed that the additional term in the denominator of Eq. (4) led to more stable training. One intuitive reason is that when $f_{\theta}(x, I)$ is the dominating term in the denominator in Eq. (4), $\nabla_{\theta} L_{\text{InfoNCE}} = 0$, so if the samples in X are poor, the gradient is zero. Without $f_{\theta}(x, I)$ in the denominator, this would not be the case.

Table 1. Distribution estimation results on SYMSOL. The table entries are estimated log likelihoods \uparrow of the true orientation averaged over 5 k test images. Results below the gray line is on our implementation of SYMSOL I. For verification, we show Ours w/o KP for both the original and our implementation of the dataset. IS: Importance Sampling. KP: Keypoints.

Method	SYMSOL I						SYMSOL II			
	avg.	cone	cyl.	tet.	cube	ico.	avg.	sphX	cylO	tetX
Prokudin et al. [25] (2018)	-1.87	-3.34	-1.28	-1.86	-0.50	-2.39	0.48	-4.19	4.16	1.48
Gilitschenski et al. [5] (2019)	-0.43	3.84	0.88	-2.29	-2.29	-2.29	3.70	3.32	4.88	2.90
Deng et al. [2] (2020)	-1.48	0.16	-0.95	0.27	-4.44	-2.45	2.57	1.12	2.99	3.61
ImplicitPDF [21] (2021)	4.10	4.45	4.26	5.70	4.81	1.28	7.57	7.30	6.91	8.49
I2S [18] (2023)	3.41	3.75	3.10	4.78	3.27	2.15	4.84	3.74	5.18	5.61
HyperPosePDF [14] (2023)	5.78	5.74	4.73	7.04	6.77	5.10	7.72	7.73	7.12	8.53
Ours w/o KP & IS	5.65	6.77	6.07	6.04	6.23	3.12	7.16	6.96	7.59	6.92
Ours w/o KP	7.33	7.62	6.46	8.69	8.63	5.23	9.27	9.07	9.32	9.41
Ours w/o KP	7.12	7.37	6.54	8.39	8.62	4.70				
Ours w/o IS	8.19	7.40	6.69	10.04	8.82	7.99				
Ours w/ cube KP	8.86	7.55	7.06	9.60	10.58	9.50				
Ours	8.97	7.67	6.96	11.04	10.10	9.06				

Table 2. Results in a low-data-regime. SYMSOL II with 10k training images instead of 45k.

Method	avg.	sphX	cylO	tetX
I2S [18] (2023)	3.61	3.12	3.87	3.84
Ours w/o KP & IS	3.95	3.56	4.68	3.60
Ours w/o KP	5.47	5.38	6.82	4.19

3.5. Inference with Pyramid Models

At inference, we evaluate a sparse tree in the pyramid to obtain most resolution where the probability is highest. First we obtain a probability distribution over the coarsest grid $x^{(0)}$. The top k poses with the highest probabilities are then expanded to the next recursion and the remaining poses become leaf nodes in the tree. This is done recursively, and after the final recursion, the sum of probabilities of leaf nodes is 1. To find the likelihood of a pose x , we find the leaf node $x_i^{(r)}$ which encompasses x , $\hat{p}(x|I) = \hat{p}(x_i^{(r)}|I)V(x_i^{(r)})^{-1}$. It is thus not detrimental if a pose is not represented at the highest resolution, since it is represented by a leaf node at a coarser resolution.

Note that when expanding poses at recursion r , the sum of the probabilities of the expanded poses in recursion $r + 1$ must be equal to the sum of the parents' probabilities in recursion r , since the sum of all leaf nodes must sum to 1. However, the relative probabilities among the expanded poses are entirely decided by the model at recursion $r + 1$, not affected by the probability at level r . This allows ambiguities at low resolution to be resolved at higher resolutions.

3.6. Network architecture

We use a UNet [27] with a ResNet18 [10] backbone to obtain a 64 dimensional feature map with the same spatial resolution as the image. From the 3D mesh of the object,

we first sample a large amount of points uniformly from the surface of the object, and reduce the set to an ordered set of 16 approximately evenly spread keypoints with farthest point sampling. Given a pose hypothesis, we then project the keypoints into the image and extract the features from the feature maps at the projected points with bilinear interpolation. Keypoints that are projected outside the image receive a learnt out-of-image embedding. The sampled keypoint features are then concatenated and fed to a three-layer MLP with 256 hidden neurons and GELU activations. The output of the network is a scalar, representing the estimated unnormalized log likelihood.

4. Experiments

We show results on SO(3) distribution estimation, comparing with previous work, and then to the best of our knowledge, we show the first quantitative results on SE(3) distribution estimation. Lastly, we argue that SE(3) distributions have many applications and show an example: multi-view pose estimation.

4.1. SO(3) results on SYMSOL

ImplicitPDF [21] introduced the synthetic dataset, Symmetric Solids (SYMSOL), for evaluation of distribution estimation in SO(3). The dataset includes a variety of geometric primitives with different kinds of symmetries. The dataset has two parts: SYMSOL I consists of a cone, a cylinder, a tetrahedron, a cube and an icosahedron, and SYMSOL II consists of a sphere, a cylinder and a tetrahedron, with a mark on each of the objects which is only visible in certain orientations, causing dynamic ambiguities.

The dataset does not include camera intrinsics or 3D models of the objects, and while the translation of the objects is fixed, the translation is unknown. Since a key part of

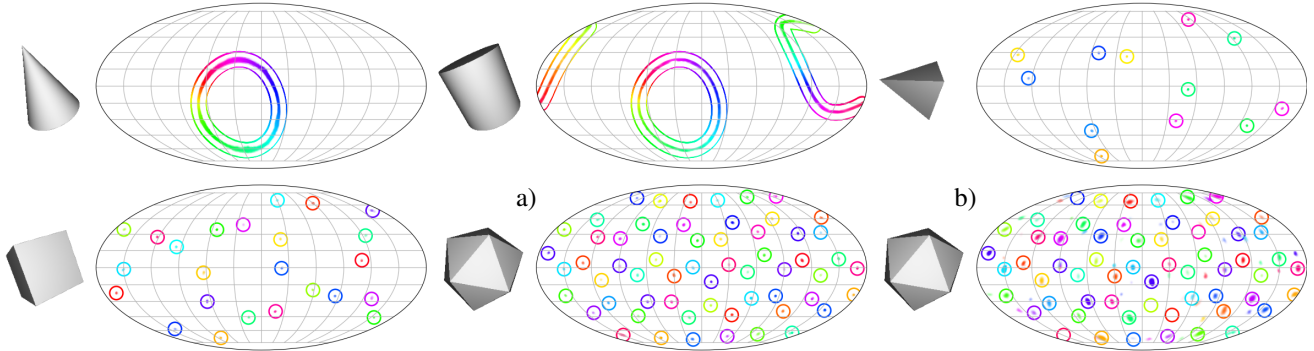


Figure 2. Qualitative SYMSOL I results. We visualize the rotations at the last pyramid level (level 6) and their likelihoods as alpha, normalized for viewing. Circles, or for continuous symmetries donut-like shapes, indicate the correct rotation up to symmetry. a) and b) are from the same image, but b) shows our method w/o KP. Our method accurately captures all 60 modes of the icosahedron. See supplementary for qualitative results on SYMSOL II.

our method is based on projection of keypoints, we cannot apply it directly to the original SYMSOL dataset. Instead, we apply a modified version of our method without keypoints on the original dataset, and implement SYMSOL I with known camera intrinsics, translation and 3D models, to evaluate our full method. We sample keypoints with farthest point sampling from the 3D model’s surface. In some cases, 3D models are not available, so we also show results where keypoints are chosen at the corners of two cubes with side lengths of 1 and 0.5 of the object diameter.

To provide results on the original dataset, we use a similar architecture as ImplicitPDF [21], with a ResNet50 [10] to obtain a latent image embedding, a positional encoding of the rotation matrix followed by a learnt projection to obtain a rotation embedding, and pass both embeddings to a small MLP. See [21] for details. While this version of our method is similar to ImplicitPDF, we still have an MLP for each level in the $SO(3)$ pyramid, and we show results with and without importance sampling.

Implementing our version of SYMSOL I, we approximately match perspective, scale and shader of the original dataset. See supplementary. SYMSOL II has textures, so it is not as easy to implement for a fair comparison.

We train object-specific models with seven MLPs ranging from $R^{(0)}$ to $R^{(6)}$, and 1024 negatives per recursion per image. For the models with importance sampling this is obtained with 128 sample trajectories, which with siblings at each recursion amounts to 1024 per MLP, because the branching factor is eight in the rotation pyramid. See Section 3.2 and 3.4. Note that while the training set contains multiple rotation annotations due to symmetry, only the first of the provided annotations per image is used during training, assuming no knowledge about the symmetries at training time. For our full method, we use a batch size of 4. Because the models without keypoints are computationally cheaper, we use a batch size of 16 for those to obtain similar training times. We use batchnorm in the MLPs for

our models without keypoints, which we found beneficial, especially for *tet.* and *ico.*. We train all our $SO(3)$ models for 50 k iterations, approximately 2 hours on a single RTX 2080 per model. The results are provided in Table 1.

We provide state-of-the-art results on SYMSOL I and SYMSOL II across all objects. Our method predicts 24 and 130 times higher likelihoods on average for the true rotation than HyperPosePDF [14] and ImplicitPDF [21], respectively. Our full method assumes that a 3D mesh is available, but our results with cube keypoints perform almost as well, getting rid of this assumption.

Using keypoints provides a big improvement. For our models without keypoints, similar to ImplicitPDF, a non-spatial latent embedding from the vision model has to express complex and high-resolution distributions in a large space. Extracting keypoint features allows the model to use the image-space as an intermediate representation of the distribution and obtain translational equivariance. In addition to translational equivariance, there are also shorter gradient pathways to the early layers in the UNet encoder, which may improve training dynamics.

Because we only evaluate a fraction of the $SO(3)$ pyramid, a distribution down to HealPix recursion 6 with 18.8 M rotations only requires 21 k evaluations with $k = 512$, almost three orders of magnitude fewer evaluations than evaluating the full grid, which allows our method to be run in real time, even on CPU. See Table 3.

While the pyramid allows us to efficiently evaluate at recursion level 6, we are also SOTA if we evaluate at recursion level 5, with avg. log likelihoods at 8.58, 8.42 and 8.80 for sphX, cylo and tetX, respectively.

Looking at Fig. 3, we see that both keypoints and importance sampling improves learning at deeper recursion levels. The log likelihood of our models without keypoints and importance sampling flattens out around recursion level 5. The figure also indicates that our models with importance sampling could improve further with a deeper pyra-

Table 3. Inference time comparison for a single image. We use $k = 512$, as in the other results. For our method we use an Intel i9-9820X CPU and an Nvidia RTX 2080 GPU. Batching improves fps further, obtaining 241 fps on SO(3) for Ours w/o KP on GPU. #eval: number of function evaluations.

Space	Method	grid size	#eval	dev.	fps
SO(3)	ImplicitPDF	2.3 M	2.3 M	gpu	2.4
	Ours w/o KP	18.9 M	21 k	cpu	16.9
				gpu	53.5
	Ours			cpu	3.3
gpu				48.3	
SE(3)	Ours	618 B	164 k	cpu	0.5
				gpu	16.1

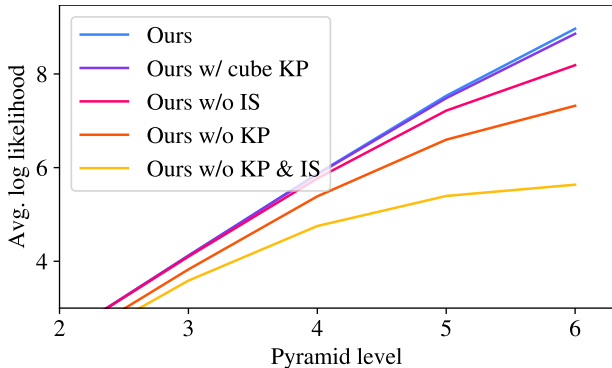


Figure 3. Log likelihoods on SYMSOL I, averaged over objects, at different recursion levels of the pyramid. Both keypoints and importance sampling improves learning at deeper levels.

mid, which is possible because of the sparse evaluation.

We note that ImplicitPDF and HyperPosePDF trains one model across all SYMSOL I objects and while we train a model per object, we use fewer function evaluations per object during training, and we provide similar improvements on SYMSOL II, where they also train a model per object.

I2S [18] reports better performance than ImplicitPDF [21] in a low-data regime, training on SYMSOL with only 10k images instead of 45k. We train our models with and without importance sampling on 9.5k of the data points, using the remaining 500 for early stopping. I2S trains ImplicitPDF’s model with 10k images with the same amount of iterations as ImplicitPDF used for 45k images, and their models have clearly overfit. Since overfitting could have easily been prevented, we believe re-reporting I2S’s results for ImplicitPDF would be unfair. Instead we note that Ours w/o KP & IS is very similar to ImplicitPDF, and similar results would be expected. The results are shown in Table 2. The experiments indicate that importance sampling improves generalization quite significantly. It is unclear as to why. On the contrary, we would expect that higher variance in the gradient without importance sampling would have had a regularizing effect.

4.2. SE(3) results on TLESS and HB

We train SE(3) pyramid models on TLESS [12] and HB [16] down to recursion level 5, selecting four objects from TLESS which represent different levels of symmetries, and four objects from HB which are common in the pose estimation community. We train on the Physically Based Renders (PBR) from [13], and show results on both held out PBR scenes as well as real images. Note that the annotations in the test set of HB are not publicly available, so we show results on the real validation set, which we did not use during training. Since we are the first to present quantitative results on SE(3) distributions, there are no baselines to compare with, but we show avg. log likelihoods for a uniform distribution on the SE(3) grid. Note that it changes slightly across objects, since the grid transformation A depends on object size and depth (See Section 3.2).

The chosen objects for TLESS have 16 k, 19 k, 23 k and 24 k images for training, and for HB: 25 k, 25 k, 24 k and 23 k. Note that we have fewer images per object than in SYMSOL, there’s a sim2real gap, and we’re attempting to learn distributions in SE(3). For the above reasons, we use heavy data augmentation during training, including random rotation, color jitter, noise and blur. We also use dropout in the MLP as well as a keypoint dropout, which zeros an entire keypoint embedding across an image. Both dropouts have a 10% chance. We use 2048 negatives per recursion corresponding to 32 trajectories through the pyramid with importance sampling. The results are presented in Table 4.

On the held out PBR images, our model predicts 220 times higher likelihood of the true pose with importance sampling than without, compared to only 2 times higher on SYMSOL I. As indicated by Fig. 3, importance sampling becomes more beneficial when the probability is more concentrated, since evaluation of uniform samples provides less and less information. On the real images, importance sampling is still beneficial, albeit not to the same degree. Some of this discrepancy is likely due to various domain gap effects such as inaccurate 3D models and inaccurate annotations. Despite the domain gap, our model predicts 25 M times higher likelihood for the annotated ground truth pose than a uniform distribution in the grid.

Fig. 4 shows examples of SE(3) distributions on TLESS. We visualize the rotational part of the SE(3) as previously. To visualize the joint distribution over position and rotation, we render leaf poses in the pyramid and weigh the renders with respect to their poses’ estimated probabilities.

4.3. Multi-view

SE(3) distributions have many potential applications. A straight forward application is multi-view pose estimation. Assuming multi-view crops and known camera extrinsics, we let $A = dI$, such that $p^{(r)}$ is a cubic grid, and use the same grid across views. Since our models have been trained

Table 4. Distribution estimation in SE(3) on four TLESS objects with different kinds of symmetries as well as four HB objects. The four HB objects are Wrench, Driller, Holepuncher and Phone, respectively. All models are trained on synthetic data (PBR), and we present results on both held out PBR data as well as real images. Entries are estimated log likelihoods of the ground truth pose, averaged over the images in the dataset. We note that we have only trained models on these eight objects, so the results should be unbiased.

Data	Method	TLESS					HB				
		avg.	1	14	25	27	avg.	2	7	9	21
PBR	Uniform	2.7	3.5	3.2	2.4	1.7	0.8	0.4	0.5	1.4	0.9
	Ours w/o IS	16.7	16.5	16.6	17.8	16.0	15.9	16.3	15.1	16.4	15.8
	Ours	21.6	22.4	20.5	22.6	20.9	21.7	21.7	21.2	21.8	21.9
Real	Uniform	2.7	3.5	3.3	2.4	1.7	0.9	0.6	0.6	1.5	1.0
	Ours w/o IS	16.6	14.1	15.9	19.2	17.2	16.0	18.6	16.5	13.2	15.8
	Ours	18.8	16.9	17.5	20.8	20.0	18.9	21.3	20.6	16.4	17.3

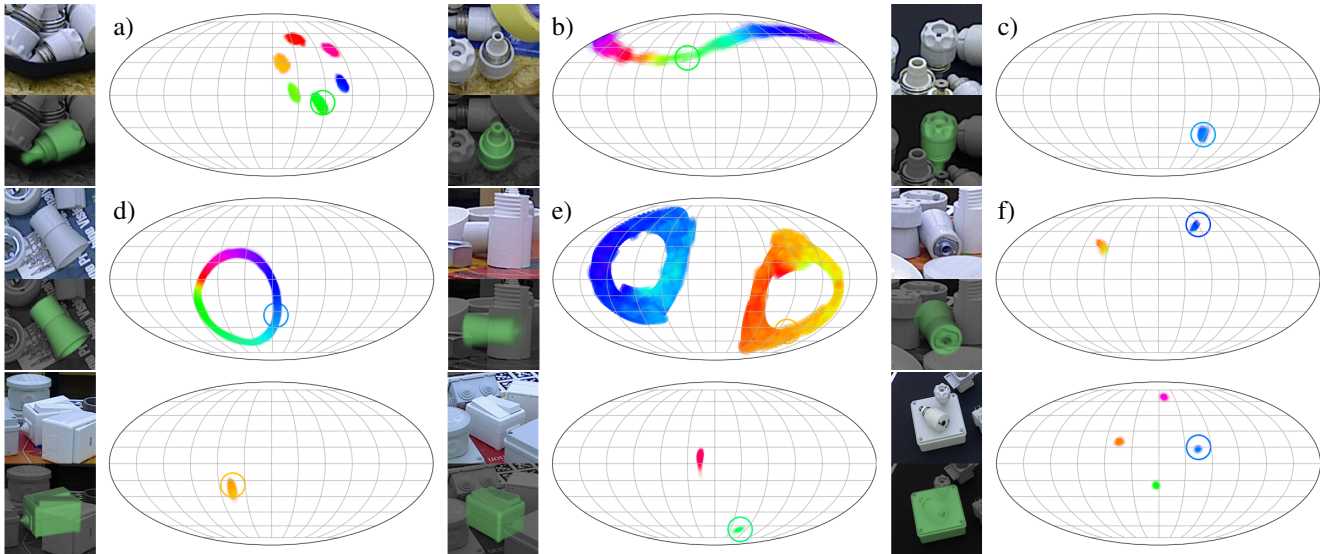


Figure 4. SE(3) distributions on TLESS. The SO(3) part of the distributions is visualized as previously. To visualize the SE(3) distribution, we show distribution renders below the original images. The first row shows three different ambiguities related to object 1. a) Discrete rotational symmetry with six modes. b) Continuous rotational symmetry. c) No symmetry. The second row shows ambiguities related to object 14. d) Continuous rotational symmetry. e) Discrete and continuous rotational symmetry. f) The continuous rotational symmetry is disambiguated by now visible features at the end of the object, and only a discrete rotational symmetry with two modes remains.

Table 5. Multi-view results on TLESS

Method	avg.	1	14	25	27
Ours	18.8	16.9	17.5	20.8	20.0
Ours w. $A = dI$	18.4	16.4	16.6	20.9	19.9
Ours + Multi-view	25.2	23.7	23.6	28.2	25.2

with randomly offset grids, we can use the same single-view models. For each recursion in the pyramid at inference, the unnormalized log likelihoods are simply averaged across views. We show multi-view pose distribution estimation results on TLESS in Table 5 with the same sets of views as in [19, 9]. We note that $A = dI$ alone do not improve performance. In fact, it can be harmful to have too much resolution along depth at inference, as most of the nodes are then “spent” on representing depth ambiguity. This simple application of our work increases the likelihood of the true pose by almost three orders of magnitude.

5. Conclusion

This work has proposed SpyroPose, a novel method for pose distribution estimation on SE(3). Our method is based on learning pose distributions at different levels of resolution using a hierarchical SE(3) grid, a pyramid, which enables importance sampling for efficient learning at training time and sparse evaluation at inference, allowing real time pose distribution estimation, even on CPU. Our method outperforms state-of-the-art methods for rotation distribution estimation on SO(3) on the SYMSOL I and SYMSOL II datasets, and to the best of our knowledge, we provide the first quantitative results on pose distribution estimation on SE(3). Lastly, we have provided an example application of our distributions, using them for multi-view pose estimation, showing great potential for our method as a core component of future work.

References

- [1] Andrea Censi. An accurate closed-form estimate of ICP’s covariance. In *2007 IEEE International Conference on Robotics and Automation*, pages 3167–3172, Apr. 2007.
- [2] Haowen Deng, Mai Bui, Nassir Navab, Leonidas Guibas, Slobodan Ilic, and Tolga Birdal. Deep bingham networks: Dealing with uncertainty and ambiguity in pose estimation. *International Journal of Computer Vision*, pages 1–28, 2022.
- [3] Xinke Deng, Arsalan Mousavian, Yu Xiang, Fei Xia, Timothy Bretl, and Dieter Fox. Poserbpf: A rao–blackwellized particle filter for 6-d object pose tracking. *IEEE Transactions on Robotics*, 37(5):1328–1342, 2021.
- [4] Marek Franaszek and Geraldine S Cheok. Propagation of orientation uncertainty of 3d rigid object to its points. In *Proceedings of the IEEE International Conference on Computer Vision Workshops*, pages 2183–2191, 2017.
- [5] Igor Gilitschenski, Roshni Sahoo, Wilko Schwarting, Alexander Amini, Sertac Karaman, and Daniela Rus. Deep orientation uncertainty learning based on a bingham loss. In *International Conference on Learning Representations*, 2019.
- [6] Krzysztof M Gorski, Eric Hivon, Anthony J Banday, Benjamin D Wandelt, Frode K Hansen, Mstvos Reinecke, and Matthia Bartelmann. Healpix: A framework for high-resolution discretization and fast analysis of data distributed on the sphere. *The Astrophysical Journal*, 622(2):759, 2005.
- [7] Frederik Hagelskjær, Aljaž Kramberger, Adam Wolniakowski, Thusius Rajeeth Savarimuthu, and Norbert Krüger. Combined optimization of gripper finger design and pose estimation processes for advanced industrial assembly. In *2019 IEEE/RSJ International Conference on Intelligent Robots and Systems (IROS)*, pages 2022–2029. IEEE, 2019.
- [8] Rasmus Laurvig Haugaard and Anders Glent Buch. Surfemb: Dense and continuous correspondence distributions for object pose estimation with learnt surface embeddings. In *Proceedings of the IEEE/CVF Conference on Computer Vision and Pattern Recognition*, pages 6749–6758, 2022.
- [9] Rasmus Laurvig Haugaard and Thorbjørn Mosekjær Iversen. Multi-view object pose estimation from correspondence distributions and epipolar geometry. *arXiv preprint arXiv:2210.00924*, 2022.
- [10] Kaiming He, Xiangyu Zhang, Shaoqing Ren, and Jian Sun. Deep residual learning for image recognition. In *Proceedings of the IEEE conference on computer vision and pattern recognition*, pages 770–778, 2016.
- [11] Tomas Hodan, Daniel Barath, and Jiri Matas. Epos: Estimating 6d pose of objects with symmetries. In *Proceedings of the IEEE/CVF conference on computer vision and pattern recognition*, pages 11703–11712, 2020.
- [12] Tomáš Hodan, Pavel Haluza, Štěpán Obdržálek, Jiri Matas, Manolis Lourakis, and Xenophon Zabulis. T-less: An rgb-d dataset for 6d pose estimation of texture-less objects. In *2017 IEEE Winter Conference on Applications of Computer Vision (WACV)*, pages 880–888. IEEE, 2017.
- [13] Tomáš Hodaň, Martin Sundermeyer, Bertram Drost, Yann Labbé, Eric Brachmann, Frank Michel, Carsten Rother, and Jiří Matas. Bop challenge 2020 on 6d object localization. In *European Conference on Computer Vision*, pages 577–594. Springer, 2020.
- [14] Timon Höfer, Benjamin Kiefer, Martin Messmer, and Andreas Zell. Hyperposepdf-hypernetworks predicting the probability distribution on so (3). In *Proceedings of the IEEE/CVF Winter Conference on Applications of Computer Vision*, pages 2369–2379, 2023.
- [15] Thorbjørn Mosekjær Iversen, Rasmus Laurvig Haugaard, and Anders Glent Buch. Ki-pode: Keypoint-based implicit pose distribution estimation of rigid objects. In *33rd British Machine Vision Conference 2022, BMVC 2022, London, UK, November 21-24, 2022*, page 222. BMVA Press, 2022.
- [16] Roman Kaskman, Sergey Zakharov, Ivan Shugurov, and Slobodan Ilic. Homebreweddb: Rgb-d dataset for 6d pose estimation of 3d objects. In *Proceedings of the IEEE/CVF International Conference on Computer Vision Workshops*, pages 0–0, 2019.
- [17] Wadim Kehl, Fabian Manhardt, Federico Tombari, Slobodan Ilic, and Nassir Navab. Ssd-6d: Making rgb-based 3d detection and 6d pose estimation great again. In *Proceedings of the IEEE international conference on computer vision*, pages 1521–1529, 2017.
- [18] David M Klee, Ondrej Biza, Robert Platt, and Robin Walters. Image to sphere: Learning equivariant features for efficient pose prediction. *arXiv preprint arXiv:2302.13926*, 2023.
- [19] Yann Labbé, Justin Carpentier, Mathieu Aubry, and Josef Sivic. Cosypose: Consistent multi-view multi-object 6d pose estimation. In *European Conference on Computer Vision*, pages 574–591. Springer, 2020.
- [20] Fabian Manhardt, Diego Martin Arroyo, Christian Rupprecht, Benjamin Busam, Tolga Birdal, Nassir Navab, and Federico Tombari. Explaining the ambiguity of object detection and 6d pose from visual data. In *Proceedings of the IEEE/CVF International Conference on Computer Vision*, pages 6841–6850, 2019.
- [21] Kieran Murphy, Carlos Esteves, Varun Jampani, Srikanth Ramalingam, and Ameesh Makadia. Implicit-pdf: Non-parametric representation of probability distributions on the rotation manifold. *arXiv preprint arXiv:2106.05965*, 2021.
- [22] Brian Okorn, Mengyun Xu, Martial Hebert, and David Held. Learning orientation distributions for object pose estimation. In *2020 IEEE/RSJ International Conference on Intelligent Robots and Systems (IROS)*, pages 10580–10587. IEEE, 2020.
- [23] Aaron van den Oord, Yazhe Li, and Oriol Vinyals. Representation learning with contrastive predictive coding. *arXiv preprint arXiv:1807.03748*, 2018.
- [24] Sida Peng, Yuan Liu, Qixing Huang, Xiaowei Zhou, and Hujun Bao. Pvnnet: Pixel-wise voting network for 6dof pose estimation. In *Proceedings of the IEEE/CVF Conference on Computer Vision and Pattern Recognition*, pages 4561–4570, 2019.
- [25] Sergey Prokudin, Peter Gehler, and Sebastian Nowozin. Deep directional statistics: Pose estimation with uncertainty quantification. In *Proceedings of the European conference on computer vision (ECCV)*, pages 534–551, 2018.
- [26] Mahdi Rad and Vincent Lepetit. Bb8: A scalable, accurate, robust to partial occlusion method for predicting the 3d

- poses of challenging objects without using depth. In *Proceedings of the IEEE international conference on computer vision*, pages 3828–3836, 2017.
- [27] Olaf Ronneberger, Philipp Fischer, and Thomas Brox. U-net: Convolutional networks for biomedical image segmentation. In *Medical Image Computing and Computer-Assisted Intervention–MICCAI 2015: 18th International Conference, Munich, Germany, October 5-9, 2015, Proceedings, Part III 18*, pages 234–241. Springer, 2015.
- [28] Guanya Shi, Yifeng Zhu, Jonathan Tremblay, Stan Birchfield, Fabio Ramos, Animashree Anandkumar, and Yuke Zhu. Fast uncertainty quantification for deep object pose estimation. In *2021 IEEE International Conference on Robotics and Automation (ICRA)*, pages 5200–5207. IEEE, 2021.
- [29] Martin Sundermeyer, Zoltan-Csaba Marton, Maximilian Durner, Manuel Brucker, and Rudolph Triebel. Implicit 3d orientation learning for 6d object detection from rgb images. In *Proceedings of the european conference on computer vision (ECCV)*, pages 699–715, 2018.
- [30] Yu Xiang, Tanner Schmidt, Venkatraman Narayanan, and Dieter Fox. Posecnn: A convolutional neural network for 6d object pose estimation in cluttered scenes. 2018.
- [31] Anna Yershova, Swati Jain, Steven M Lavelle, and Julie C Mitchell. Generating uniform incremental grids on $so(3)$ using the hopf fibration. *The International journal of robotics research*, 29(7):801–812, 2010.